DISCLAIMER

ORNL/TM-2024/3606

Nanostructured Alumina-Forming Austenitic Alloy (NAFA) Production Using Advanced Manufacturing

Tim Graening
Caleb Massey
David Hoelzer
Yukinori Yamamoto
Holden Hyer
Josh Kendall
Xiao-Ying Yu
Gabriel Parker
Sebastien Dryepondt

September 2024

M3FT-24OR060101033

OAK RIDGE National Laboratory

ORNL IS MANAGED BY UT-BATTELLE LLC FOR THE US DEPARTMENT OF ENERGY

ORNL/TM-2024/3606

Innovative Nuclear Materials Program

NANOSTRUCTURED ALUMINA-FORMING AUSTENITIC ALLOY (NAFA) PRODUCTION USING ADVANCED MANUFACTURING

Tim Graening
Caleb Massey
David Hoelzer
Yukinori Yamamoto
Holden Hyer
Josh Kendall
Xiao-Ying Yu
Gabriel Parker
Sebastien Dryepondt

September 2024

M3FT-24OR060101033

Prepared by
OAK RIDGE NATIONAL LABORATORY
Oak Ridge, TN 37831
managed by
UT-BATTELLE LLC
for the
US DEPARTMENT OF ENERGY
under contract DE-AC05-00OR22725

CONTENTS

LIST OF FIGURES

LIST OF TABLES

ACKNOWLEDGMENTS

This research was sponsored by the US Department of Energy Office of Nuclear Energy's Innovative Nuclear Materials Program under contract DE-AC05-00OR22725 with UT-Battelle LLC. One of the alloys analyzed in this work was originally developed under the Powertrain Materials Core Program, Vehicle Technologies Office, Office of Energy Efficiency and Renewable Energy. The authors thank Dr. Samuel Bell for his thoughtful review of this report before publication. The authors would also like to thank Daniel Newberry and Jim Horenburg for their assistance with sample preparation.

ABSTRACT

Alumina-forming austenitic (AFA) alloys are well known for their exceptional corrosion-resistant properties due to the formation of a dense oxide scale beneficial in their application as a nuclear material. However, use of the alloys in core material applications is limited due to the high nickel-transmutation and helium generation rate in service, leading to swelling and reduced lifetimes. Enhancing the sink strength to pin gas bubbles and increasing gas management of the material may mitigate many of the degradation phenomena expected during alloy deployment (such as high-temperature helium embrittlement and cavity swelling for lead-cooled fast-reactor applications). Nanostructured materials are usually produced using a time-consuming and expensive batch process like mechanical alloying to achieve the fine homogenous distribution of nanoprecipitates throughout the matrix material. Integrating the nanoprecipitates in modern additive manufacturing processes has proven difficult, as the required nano-sizes or number densities cannot be achieved simultaneously. Efforts to increase the number density of precipitates by adding more precipitate-forming rare-earth elements led to agglomeration of such elements, while the nano-sized precipitates did not form in sufficient quantity when not enough rare-earth element was use. In this work a novel approach to advanced manufacturing and the fabrication of Nanostructured AFA (NAFA) materials was chosen. A dual precipitate-forming NAFA steel with a chemistry more suitable for advanced reactor applications was produced to create an environmentally resistant, high-sink-strength austenitic alloy for advanced reactor cladding applications.

1. INTRODUCTION

Alumina-forming austenitic (AFA) stainless steels are a class of fully face-centered cubic (FCC) iron-based alloys designed for use in extreme environments requiring oxidation resistance at high temperatures. Originally designed in the early 2000s for use in fossil power generating systems (boiler tubing, steam turbine components, etc.), this class of alloys was designed with increased levels of aluminum to form a passive aluminum oxide scale instead of the conventional chromium oxide scales normally formed on conventional stainless steels [1]. These alloys also have higher creep strength in comparison with conventional ferritic or ferritic/martensitic alloys, making them particularly suitable for higher-temperature service.

Due to these beneficial characteristics, AFAs may provide similar performance benefits in nuclear applications. For low-dose applications, AFAs have recently been funded under the Gateway for Accelerated Innovation in Nuclear (GAIN) initiative, where oxidation-resistant AFAs were scoped for use as a high-temperature structural material in lead-cooled fast-reactor conditions [2]. Some scoping of wrought AFAs in the Advanced Fuels Campaign was also done to assess their relevance as an accident-tolerant fuel cladding candidate for light water reactors [3].

Although austenitic alloys have high-temperature mechanical properties that are superior to their ferritic variants, the FCC crystal structures are more susceptible to cavity swelling at fast-reactor operating temperature regimes. This issue can be partially resolved by increasing the relative sink strength of austenitic alloys by engineering alloys to have a high density of secondary phases to absorb and annihilate irradiation-induced defects. It is for this reason that alloys such as cold-worked D9 (a form of titanium-stabilized 316 stainless steel) became popular as a fast-reactor cladding candidate 50 years ago, since the formation of nanoscale TiC precipitates was shown to significantly reduce cavity swelling at fast-reactor operating temperatures (350–550°C). In fact, other advanced austenitic alloys developed internationally, such as Japan's PNC316 alloy, also showed less than 3% volumetric swelling after irradiation up to 110 dpa in their JOYO fast reactor [4].

The design of high-sink-strength oxide dispersion–strengthened (ODS) AFA variants is thus pursued in this work package for eventual tube production for irradiation-resistant fuel cladding production. A previous report [5] outlined the design strategy, which includes (1) thermodynamic and neutronic design of AFAs with reactor-specific compositions, (2) demonstration of laboratory-scale NAFA production using conventional ODS alloy fabrication technologies, and (3) expansion of the NAFA processing window by using advanced manufacturing. Previous work on conventional production of NAFAs resulted in high-volume fractions of intermetallic phases, which decreased alloy performance at high temperature, but nanoscale precipitation was demonstrated after extensive mechanical alloying and consolidation [6]. To further improve on the performance of these alloys, this report summarizes NAFA production using rapid solidification via laser-powder bed fusion. The microstructure, high-temperature stability, and mechanical properties of proof-of-concept prints are summarized in this report, with future research thrusts identified for FY25.

2. MATERIALS AND METHODS

2.1 Material Selection of Novel Nanostructured Alumina-Forming Austenitic Steel

Additive manufacturing has been researched over the past decade to offer an alternative route for scalable economically viable production of ODS steels [7]. The required nano-scaled precipitate sizes were producible using gas atomization reaction synthesis (GARS). However, the success of that research was limited, as the process was unable to produce high number densities for those nano-scaled precipitates $>10^{22}$ m^{-3}. An increase of the nanoprecipitate-forming elements led to growth of the nanoprecipitates but not an increase of the number density, which remained one to two to three orders of magnitude below the conventionally manufactured ODS steels [8–10]. The number of nanoscale precipitates is important to increasing high-temperature creep performance and acts as a sink for irradiation-induced defects [11–13].

To overcome the issue of a low number density of precipitates, while keeping the size of oxide precipitates in the intended range between 2 and 20 nm, it is theorized that sequestering of an oxygen-independent second phase of precipitates could potentially increase the total sink strength to conventional ODS steel levels. To achieve that, the pre-alloy composition was changed to enable the formation of a second-phase precipitate. Elements capable of forming small-scaled precipitates which do not interfere with the oxide precipitate formation have been evaluated, and the composition was adjusted to reflect that. Nitrides were chosen as the preferred precipitates, with zirconium as the major element to react with nitrogen. Further optimization steps and lesson learned from the first generation of trials were applied. For example, niobium content was increased to capture carbon and to help with oxidation resistance of the matrix, improving creep-rupture life.

Additive manufacturing itself will be performed under a nitrogen-containing atmosphere, with 5% oxygen to foster ODS precipitate formation, while enabling the formation of nitrides as a second phase. The final composition for a new NAFA alloy is shown in Table 1. The chromium content was decreased to avoid a sigma phase formation, while nickel was increased to cover the reduced carbon content. Carbon content was reduced to decrease the amount of large $M_{23}C_6$ precipitates, as they tend to grow rapidly during annealing and operating conditions. The content of molybdenum was increased as a solution strengthening element, and tungsten was eliminated. Manganese was reduced to a minimum as it can compromise the continuous alumina scale. The resulting phase diagram is presented in Fig 1 without the impact from the GARS process and the addition of nitrogen and oxygen to form precipitates.

Table 1. Specified chemical compositions of the novel NAFA-2 powder in comparison with the previous generation of NAFA-1. The compositions are in weight percent as provided in supplier material certifications.

Element	NAFA-2				NAFA-1
	Target (wt %)	Target Min (wt %)	Target Max (wt %)	Measured (wt.%)	Supplier Certificate
Fe	**Bal.**	Bal.	Bal.	Bal.	Bal.
Cr	15	14.5	15.5	15.17	23.0
Mn	0.2	0.1	0.3	0.25	2.0
Ni	25	24.5	25.5	25.31	23.0
Cu	-	-	0.1	0.009	-
Al	3.75	3.5	4	3.58	4.0
Si	0.2	0.1	0.3	0.2	0.4
Nb	1.5	1.3	1.7	1.37	0.7
Mo	2	1.8	2.2	1.98	0.98
W	-	-	0.1	0.004	0.5
Zr	0.18	0.16	0.2	0.21	0.13
C	-	-	0.05	0.007	0.5
B	-	-	0.01	<0.001	0.01
N	-	-	0.03	0.029	0.04
Y	0.13	0.13	0.17	0.13	0.10

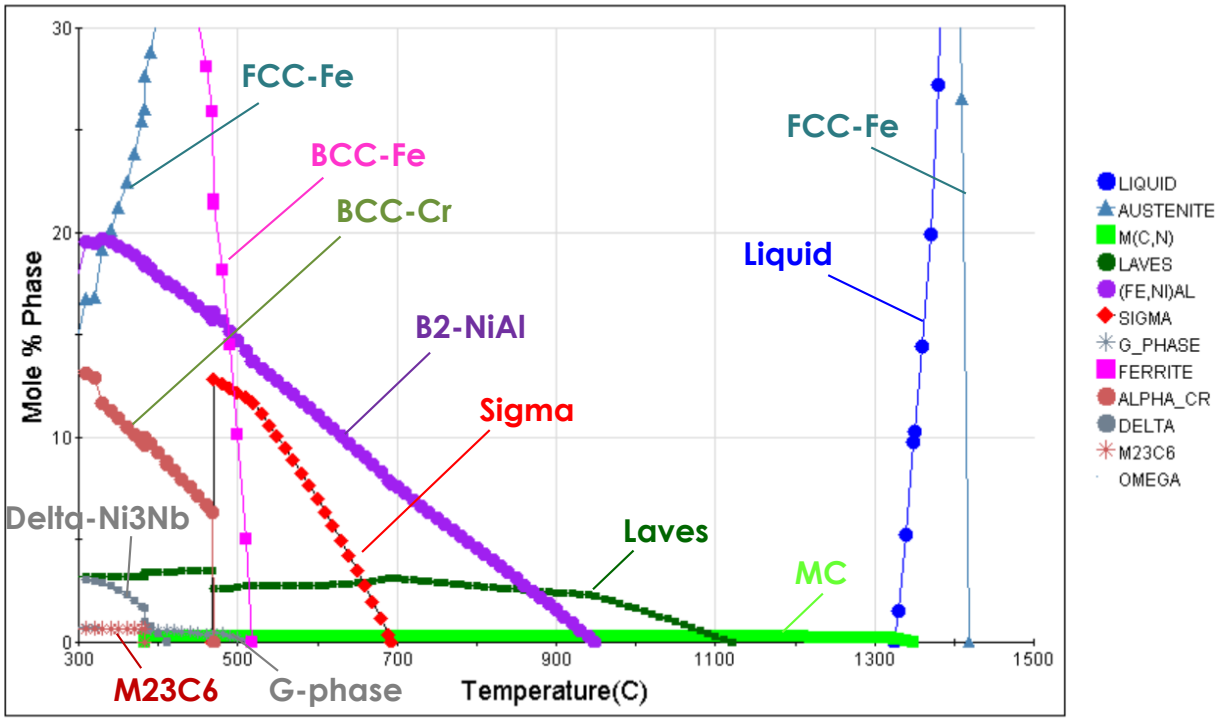

Fig 1. Phase diagrams for NAFA-2 gas atomized powder.

2.2 Microscopy Methods

Investigation of the microstructure was performed via scanning electron microscopy (SEM) and transmission electron microscopy (TEM). SEM was performed using a MIRA 3 SEM by TESCAN USA, Inc., equipped with an Oxford Symmetry electron backscatter detector (EBSD) using a probe current of around 3–6 nA. All EBSD data were collected using a 20 kV accelerating voltage with a 6–8 nA beam current. TEM specimens were prepared using standard focused ion beam (FIB) preparation. Lift-out of a bulk sample with a length of around 15 microns was performed, before it was subsequently thinned to a thickness of around 120 nm in the regions of interest. TEM was performed using an FEI (now Thermo Fisher Scientific, Waltham, MA, USA) Talos F200X scanning transmission electron microscope (S/TEM) operating at 200 kV. Energy dispersive X-ray spectroscopy (EDS) was used to map element distributions across various magnifications to capture nanoscale and microscale precipitates. Mappings were completed using a probe current of ~1 nA and a probe size of less than 1 nm with active drift correction every 30 s. The spectrum images were recorded using a 1024 × 1024 pixels region with a 3 × 3 neighborhood averaging filter applied during image post-processing to increase signal. Scan duration for each map was between 45 and 90 minutes.

2.3 Additive Manufacturing of NAFA-2 via Laser Powder Bed Fusion

Laser powder bed fusion (LPBF) is additive manufacturing techniques that involves the selective laser melting of a powder bed, melting, and fusing material together in a layer-by-layer manner, as shown in Fig. 2. There are multiple processing parameters that can be adjusted, effectively changing the total energy input into the system. Some of the most influential parameters include the laser power (p), the raster scan speed of the laser (v), the distance between consecutive laser scans (i.e., hatch spacing, h), and the powder layer thickness (lt). These parameters can be normalized into a volumetric energy density (ED) term:

$$ED = \frac{p}{v \times h \times lt}. \tag{1}$$

For pulsed laser systems, such as the one used in this study, the laser does not follow a scan speed but rather a switching on/off and jumping between points; an effective scan speed can be calculated as follows:

$$v = \frac{pd}{dt + t}, \tag{2}$$

where pd is the point distance, dt is the dead time of the laser (hard wired at 10 µs), and t is user input dwell time at each point.

The gas-atomized NAFA-2 alloy powder was processed using a Renishaw AM400 LPBF system. The AM400 is equipped with a ytterbium-fiber pulsed laser having a spot size and wavelength of ~70 and 1.070 µm. A design of experiments (DOE) approach was used to systematically vary the laser power, scan speed (dwell time and point distance), and the hatch spacing following the energy density equation in Eq. (1). The layer thickness was set constant at 30 µm, based on previous work with processing AFA alloys. A linear hatch vector strategy was applied for scanning the powder bed setting—the scan rotation between layers was at 67°, width

between consecutive stripes boundaries at 5 mm, and a hatch offset of 60 µm for overlapping between stripes.

A central composite design (CCD) DOE was used since it limits user bias for parameter selection, requiring a high and low value for each parameter to be varied. The CCD follows a statistical regression, allowing squared terms, so that fitted response data regression is quadratic and more accurate than a typical factorial or Taguchi design. All CCD designs were generated using the Minitab statistical software (v. 21). Varying four parameters in a CCD produces 30 separate parameter combinations per processing (P) study, i.e., PA, PB, PC, and PD. An initial study, PA, was performed in ultra-high-purity (UHP) argon to first evaluate the processing behavior of the NAFA-2 alloy before printing in reactive atmospheres. The first set of parameters was based around the optimized parameter for a different AFA composition printed previously and is reported in Table 1. As will be shown later, the NAFA-2 alloy behaved differently from expected, requiring an adjustment of the processing parameters for studies PB and PC in the reactive atmospheres. Study PD had the same parameters as PB and PC but was performed in UHP argon.

Simple cubic geometries having a cross section of 5 mm × 10 mm were fabricated 12 mm tall. The bottom 2 mm were considered sacrificial during removal from the build plate via a diamond wire saw. After build plate removal, the volumetric density was measured via the Archimedes immersion method as described in ASTM B962. The cubes were floated in ethanol at room temperature (~25°C), and three measurements were taken for each cube. Parameters and the resulting Archimedes density for the study PA and studies PB, PC, and PD are reported in Tables 2 and 3, respectively. Without having to report it for all samples, the standard deviation in the Archimedes measurements was < 0.015 g/cm^3 for all cubes.

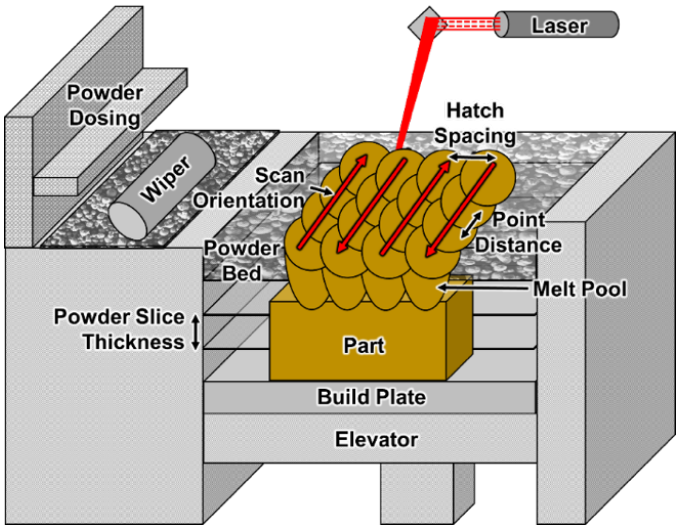

Fig. 2. Schematic of a typical LPBF build chamber and the overall process.

Table 2. LPBF processing parameters and resulting Archimedes density for the cubes printed in study PA under UHP argon.

Number	Power (W)	Point Distance (μm)	Dwell Time (μs)	Hatch Spacing (μm)	Layer Thickness (mm)	Scan Speed (mm/s)	Energy Density (J/mm^3)	Archimedes Density (g/cm^3)
1	150	50	140	100	0.03	333.3	150.0	7.34
2	250	70	140	100	0.03	466.7	178.6	7.43
3	250	50	140	120	0.03	333.3	208.3	7.37
4	200	60	120	110	0.03	461.5	131.3	7.42
5	150	70	100	100	0.03	636.4	78.6	**7.54**
6	200	60	120	110	0.03	461.5	131.3	7.42
7	250	70	100	120	0.03	636.4	109.1	7.50
8	150	70	140	120	0.03	466.7	89.3	7.47
9	150	50	100	120	0.03	454.5	91.7	7.47
10	250	50	100	100	0.03	454.5	183.3	7.45
11	250	70	100	100	0.03	636.4	131.0	7.52
12	150	50	140	120	0.03	333.3	125.0	7.36
13	250	70	140	120	0.03	466.7	148.8	7.46
14	150	70	140	100	0.03	466.7	107.1	7.46
15	200	60	120	110	0.03	461.5	131.3	7.42
16	250	50	140	100	0.03	333.3	250.0	7.36
17	150	50	100	100	0.03	454.5	110.0	7.45
18	250	50	100	120	0.03	454.5	152.8	7.47
19	200	60	120	110	0.03	461.5	131.3	7.42
20	150	70	100	120	0.03	636.4	65.5	7.52
21	200	80	120	110	0.03	615.4	98.5	7.48
22	200	60	120	130	0.03	461.5	111.1	7.44
23	200	60	160	110	0.03	352.9	171.7	7.32
24	200	40	120	110	0.03	307.7	197.0	7.31
25	100	60	120	110	0.03	461.5	65.7	7.54
26	200	60	80	110	0.03	666.7	90.9	7.52
27	200	60	120	110	0.03	461.5	131.3	7.42
28	300	60	120	110	0.03	461.5	197.0	7.46
29	200	60	120	110	0.03	461.5	131.3	7.42
30	200	60	120	90	0.03	461.5	160.5	7.39

Table 3. LPBF processing parameters and resulting Archimedes density for the cubes printed in studies PB, PC, and PD under different atmospheres.

Number	Power (W)	Point Distance (μm)	Dwell Time (μs)	Hatch Spacing (μm)	Layer Thickness (mm)	Scan Speed (mm/s)	Energy Density (J/mm^3)	Archimedes Density (g/cm^3)		
								PB	PC	PD
Build Atmosphere								90%Ar/5% N_2/5%O_2	75%Ar/20% N_2/5%O_2	100 %Ar
1	200	90	130	100	0.03	642.9	103.7	7.51	7.59	7.51
2	150	70	100	110	0.03	636.4	71.4	7.51	7.59	7.54
3	100	50	70	120	0.03	625.0	44.4	7.14	7.23	7.32
4	100	90	130	120	0.03	642.9	43.2	7.20	7.29	7.36
5	200	90	70	120	0.03	1125.0	49.4	7.41	7.50	7.52
6	100	90	70	100	0.03	1125.0	29.6	6.86	6.93	6.78
7	200	50	70	100	0.03	625.0	106.7	7.50	7.57	7.53
8	100	50	130	100	0.03	357.1	93.3	7.53	7.59	7.53
9	150	70	100	110	0.03	636.4	71.4	7.50	7.57	7.54
10	200	50	130	120	0.03	357.1	155.6	7.38	7.37	7.33
11	150	70	100	110	0.03	636.4	71.4	**7.51**	**7.58**	7.54
12	200	90	130	120	0.03	642.9	86.4	7.48	7.55	7.51
13	100	90	130	100	0.03	642.9	51.9	7.47	7.54	7.50
14	100	50	70	100	0.03	625.0	53.3	7.45	7.53	7.49
15	100	90	70	120	0.03	1125.0	24.7	6.89	6.96	6.91
16	100	50	130	120	0.03	357.1	77.8	7.51	7.58	7.55
17	150	70	100	110	0.03	636.4	71.4	7.49	7.57	7.54
18	200	50	70	120	0.03	625.0	88.9	7.47	7.55	7.53
19	200	90	70	100	0.03	1125.0	59.3	7.49	7.57	7.53
20	200	50	130	100	0.03	357.1	186.7	7.26	7.36	7.27
21	150	70	100	110	0.03	636.4	71.4	7.48	7.58	7.53
22	150	110	100	110	0.03	1000.0	45.5	7.43	7.52	7.51
23	150	30	100	110	0.03	272.7	166.7	7.20	7.31	7.23
24	50	70	100	110	0.03	636.4	23.8	6.96	6.99	6.79
25	250	70	100	110	0.03	636.4	119.0	7.47	7.56	7.53
26	150	70	40	110	0.03	1400.0	32.5	6.86	6.90	6.86
27	150	70	100	90	0.03	636.4	87.3		7.59	7.55
28	150	70	160	110	0.03	411.8	110.4	7.40	7.50	7.41
29	150	70	100	130	0.03	636.4	60.4	7.49	7.57	7.54
30	150	70	100	110	0.03	636.4	71.4	7.50	7.59	7.55

Archimedes density data for the study PA were plotted against similar data taken for the AFA05 alloy in Fig. 3(a). The optimized parameter from the AFA05 Archimedes data had an energy density of ~131 J/mm^3. Designing the CCD for processing NAFA-2 in study PA was centered around the ~131 J/mm^3 parameter. However, as can be seen more easily in Fig. 3(b), the NAFA-2 exhibited higher density at lower energy densities. Therefore, the parameters for PB, PC, and PD were adjusted to more readily observe the evolution of density during LPBF processing of the NAFA-2 alloy.

Archimedes density data for the three studies PB, PC, and PD processed under a 90% Ar - 5% N_2 - 5% O_2, 75% Ar - 20% N_2 - 5% O_2, and 100% Ar (UHP Ar) atmosphere, respectively, are shown in Fig. 3(c). Overall, all studies exhibited similar trends in the density as a function of energy density. The highest densities were achieved in study PC under the 75% Ar - 20% N_2 - 5% O_2 atmosphere; however, Archimedes is prone to error due to limitations with penetrating internal porosity/voids, so no major conclusion can be made that NAFA-2 printed better in one particular atmosphere from the density data.

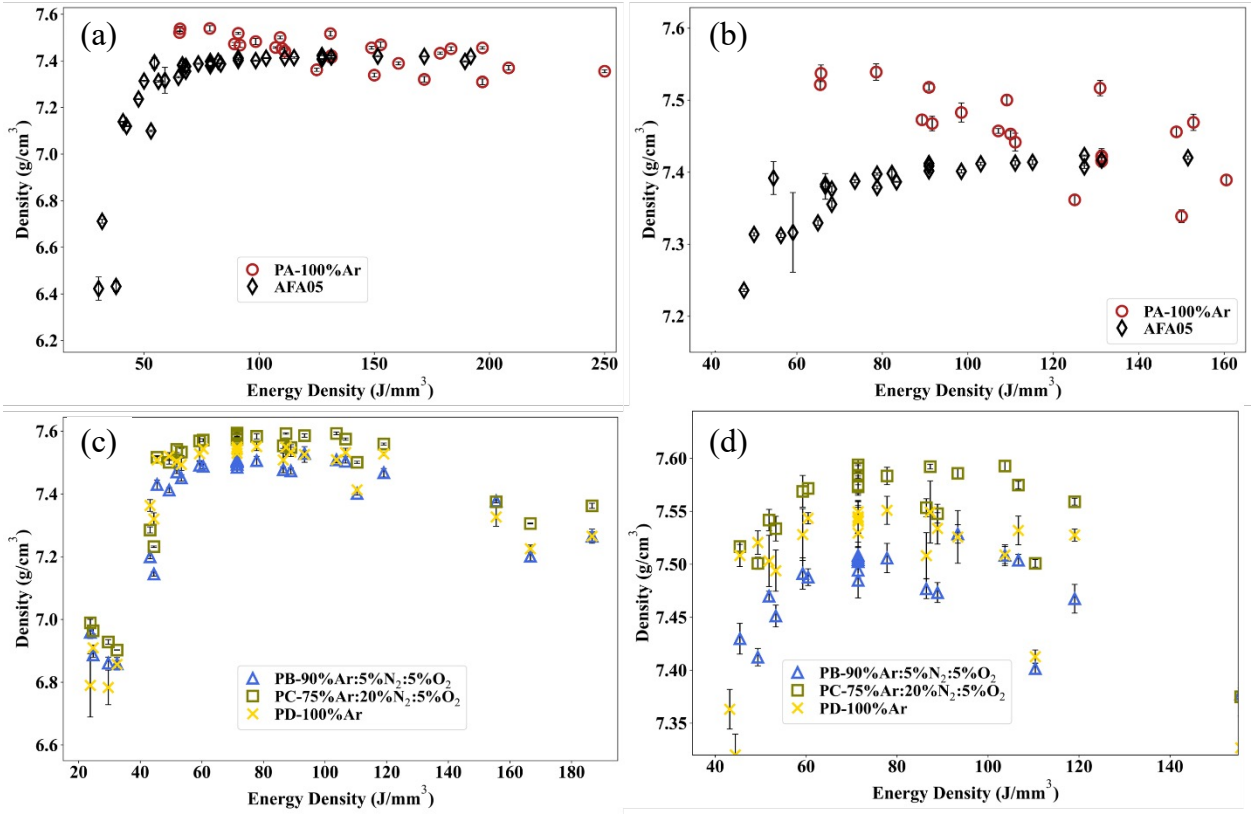

Fig. 3. Archimedes density data for the (a,b) previously processed AFA05 alloy and the study PA and (c,d) studies PB, PC, and PD processed under a 90%Ar:5%N_2:5%O_2, 75%Ar:20%N_2:5%O_2, and 100%Ar (UHP Ar) atmosphere, respectively. Data included for (a,c) all samples and (b,d) focused around the highest densities achieved.

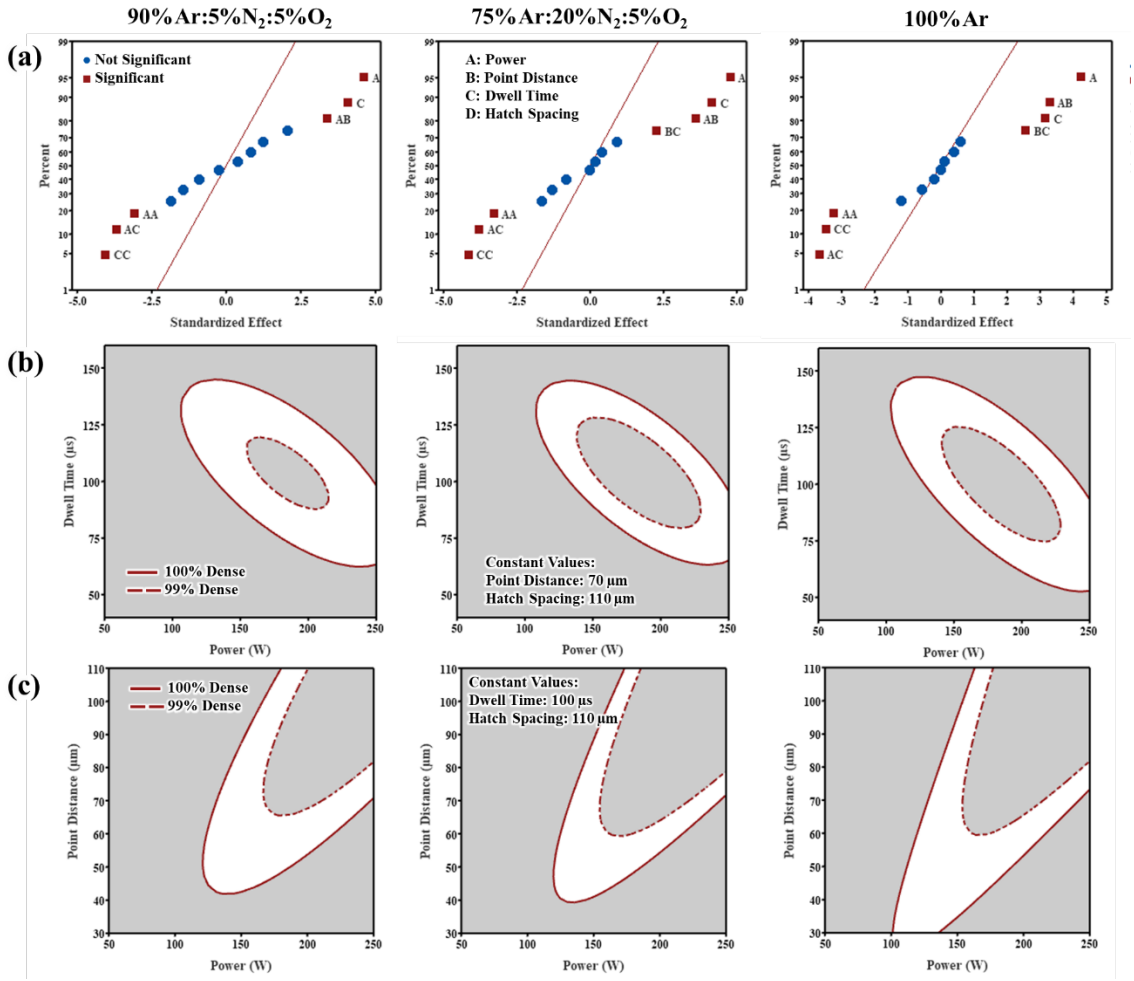

Fig. 4. (a) Normalized regression fitting of the Archimedes density and (b,c) process mappings for the studies PB, PC, and PD, processed under the 90%Ar:5%N_2:5%O_2, 75%Ar:20%N_2:5%O_2, and 100%Ar (UHP Ar) atmospheres, respectively. (a) Normalization curves indicated specific parameters and interactions that are considered statistically significant to the Archimedes density response data. (b,c) The drawn solid and dashed curves indicate the region of space where material >99% dense can be achieved as a function of (b) laser power and dwell time and (c) laser power and point distance.

To provide some context for optimization, the Archimedes density data were analyzed using the statistical software Minitab, and some select results are shown in Fig. 4. Response data such as the Archimedes density can be reread into the Minitab and processed using the prescribed CCD. Statistical significance is assigned to parameters, or interactions between two parameters, based on their unbiased effect on the response data. The normalized plots in Fig. 4(a) indicate that the laser power and dwell time are most influential independent parameters, and the most influential interactions are between laser power and point distance/dwell time for all three atmospheres. Process maps were then generated between the laser power and Fig. 4(b) dwell time and Fig. 4(c) point distance, respectively. The solid lines in Fig. 4(b,c) indicate the hard line where the highest Archimedes density was achieved, and the dashed lines indicate the density at which only 99% dense material is achieved, leaving a white space between the two to indicate the processing window for the alloy. Overall, the process mappings are similar for all three atmospheres, with a small indication that higher densities could potentially be achieved in 100% argon.

Twelve samples from the PA, PB, and PC study were cross-sectioned and metallographically prepared for confirmation of defects and total void space in the samples for comparison with Archimedes density data. Optical images of the cross section (parallel with the build direction) are shown for studies PA, PB, and PC in Fig. 5 as a function of energy density. Overall, use of lower energy densities results in a lack of fusion between particles, creating irregular pores, whereas excessive energy densities boil the melt, causing the formation of more spherical porosity. There appears to exist a middle point at ~71 J/mm^3 where porosity is minimized and high densities are indeed achieved as previously indicated by the Archimedes density data. However, there is clear indication of solidification cracking at all parameters, regardless of process atmosphere. Cracking does appear limited for samples PA-5 (79 J/mm^3) and at the optimized 71 J/mm^3 for samples PB-11 and PC-11. Any cracking in the as-built microstructure will most likely be detrimental but may only slightly affect the materials performance.

Even though cracking was observed, dense material was fabricated for the NAFA-2 alloy under the reactive atmospheres. Therefore, the densest samples were analyzed using SEM and TEM to observe microstructural changes and determine the potential presence of oxides and nitrides.

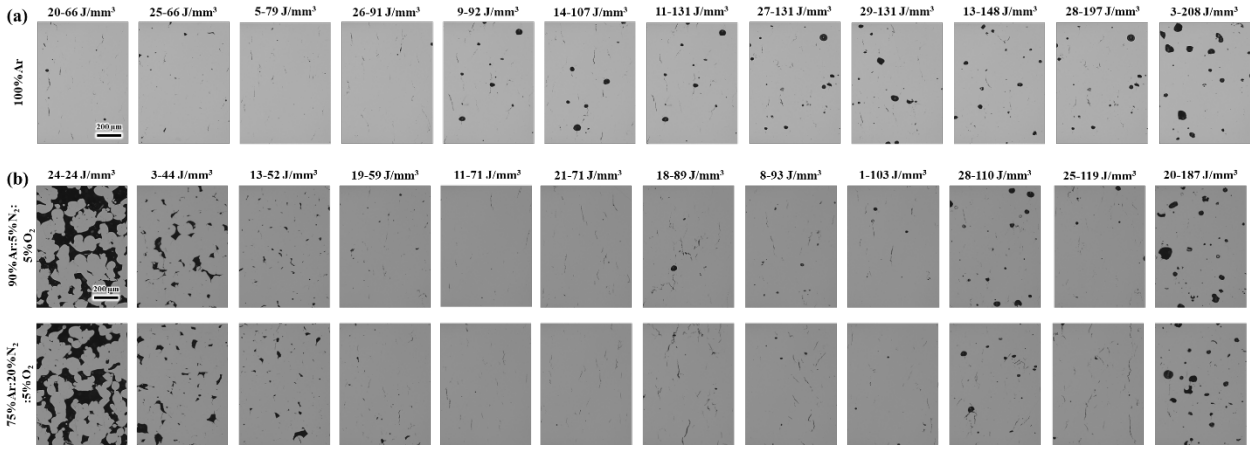

Fig. 5. Optical images of the cross-sectioned samples selected from studies (a) PA and (b) PB and PC. Images are arranged as a function of energy density, low to high reading left to right. The build direction is parallel with the height of the image, bottom to top.

3. MICROSTRUCTURAL EVALUATION OF LPBF NAFA BUILDS

Microstructures of conventional hot isostatic pressing (HIP-AFA) and mechanically alloyed NAFA-1 were investigated in detail and published in a report earlier this year [6]. Here, dual precipitation of oxides and nitrides via LPBF under a nitrogen-rich atmosphere was attempted as a proof-of-concept study. Samples PA-05, PB-11, and PC-11 (see marked in green in Tables 2 and 3) were selected for further investigation due to their high density close to the theoretical density and their ease of printability. The same blocks after printing are shown in Fig 6 with optical images of cut samples showing small cavities and minor cracking, as mentioned above. Those cracks parallel to the build direction are visible for all samples independent of the selected printing atmosphere. An increased preheat temperature could potentially help reduce the thermal gradient during printing which could cause cracking. Outside of process parameters, a slight adaptation to the chemical composition might be required to reduce the sigma, laves, and B2 phase fraction slightly while keeping the niobium content high enough to form a protective alumina scale via LPBF.

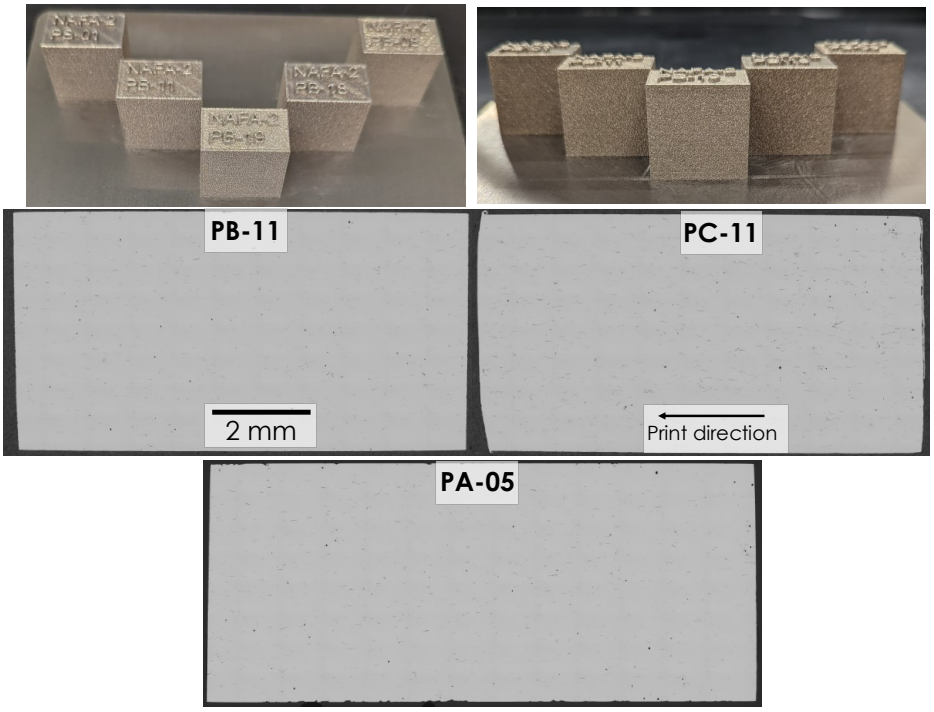

Fig 6. Photographs of the printed PB and PC sample cubes and optical images of the cut and polished samples of PB-11, PC-11, and PA-05. All of the samples show small cavities and some minor cracking traversing from left to right.

Inverse pole figure (IPF) maps are shown in Fig 7 with the build direction (BD) from bottom to top that reveal very similar microstructures across all three samples and indicate no direct impact of the printing atmosphere on grain size or texture. Maps at higher magnifications also did not show a measurable difference. To investigate the impact of the printing atmosphere, quantitative chemical analysis of the minor elements on the material was performed by the DIRATS Laboratory using combustion and inert gas fusion (IGF) for carbon and for oxygen and nitrogen, respectively, as presented in Fig 8. An increase in nitrogen content in the additive manufacturing atmosphere for PA, PB, to PC was used with 5% of oxygen in PB and PC. That would suggest that the oxygen levels should be increased in PB and PC in comparison with PA, but that is not the case. Only PC shows around double the measured oxygen content, with PB actually showing a slightly lower level of oxygen than PA. Nitrogen contents are very similar across all three samples, with a slight nitrogen increase from PA to PB and PC. However, that increase was anticipated to be significantly larger than the measured one.

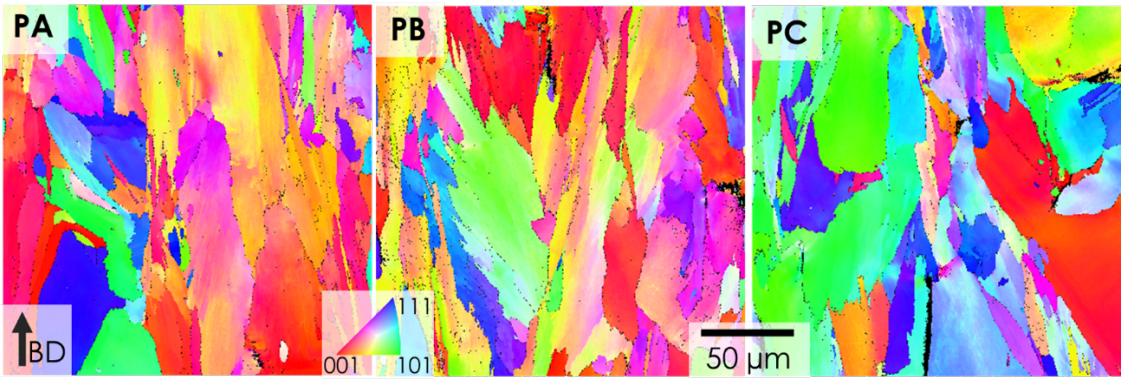

Fig 7. IPF maps of PA, PB, and PC samples with the same magnification show no difference in microstructure and grain size.

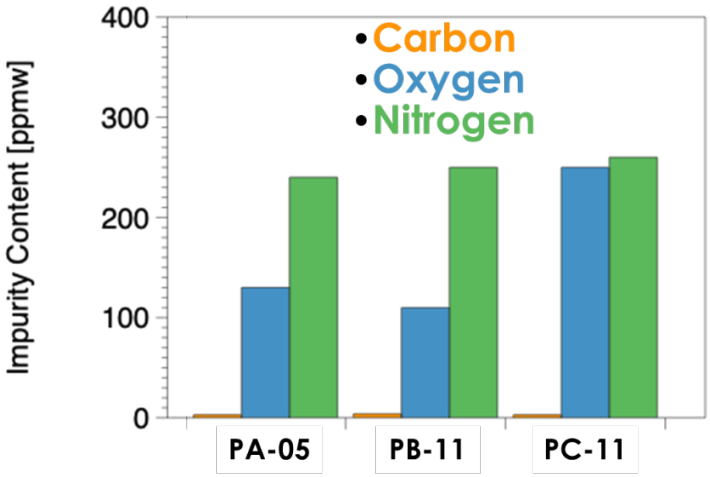

Fig 8. Chemical analysis performed by DIRATS Laboratories of PA-05, PB-11, and PC-11 for minor elements shows a doubled oxygen content in PC-11 in comparison with the other two samples, while only an insignificant increase in nitrogen is shown for PB and PC.

To verify the chemical analysis findings, Time-of-Flight Secondary Ion Mass Spectrometry (ToF-SIMS) depth profiling experiments were conducted. An example of depth profiling data of sample PA-05 is shown in Fig 9. In comparison with sample PA-05 printed under argon, the profile of sample PC-11, printed under 20% N and 5% O, is displayed in Fig 10, clearly indicating that less argon was implemented during printing in a partial nitrogen- and oxygen-rich atmosphere. A ranking regarding the abundance of elements is shown next to the depth profile of PC-11 in Fig 10. The results agree with the trend of an increase in nitrogen from PA to PC but are not in agreement regarding the measured oxygen levels.

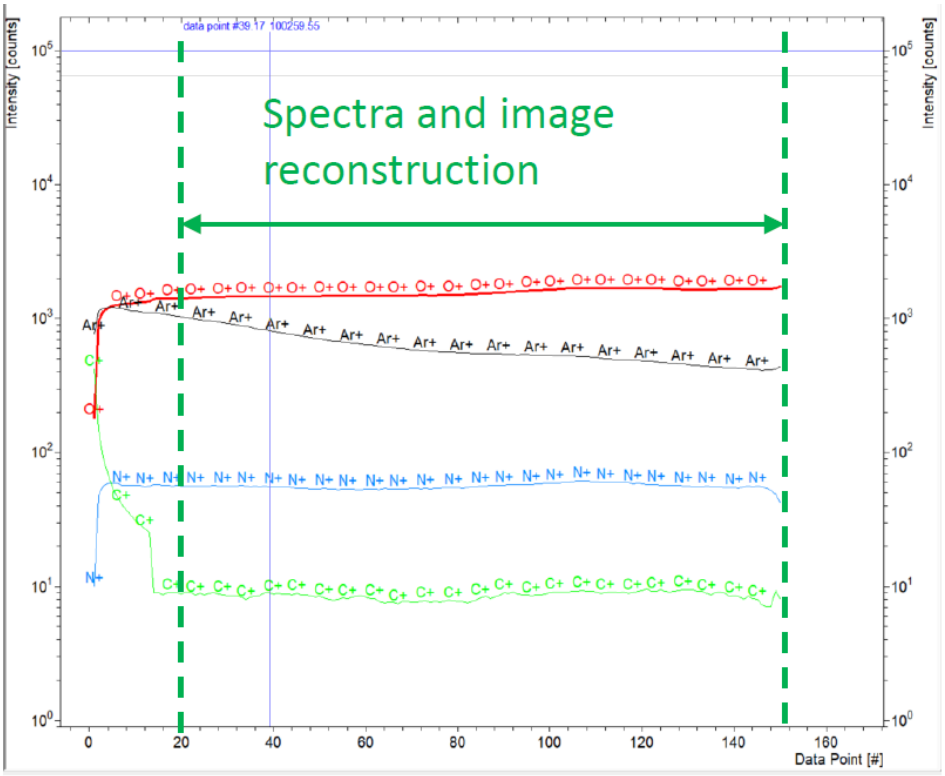

Fig 9. TOF-SIMS depth profile of O+, Ar+, N+, and C+ in sample PA-05. Spectra and image reconstruction was in the marked area to reduce surface impact.

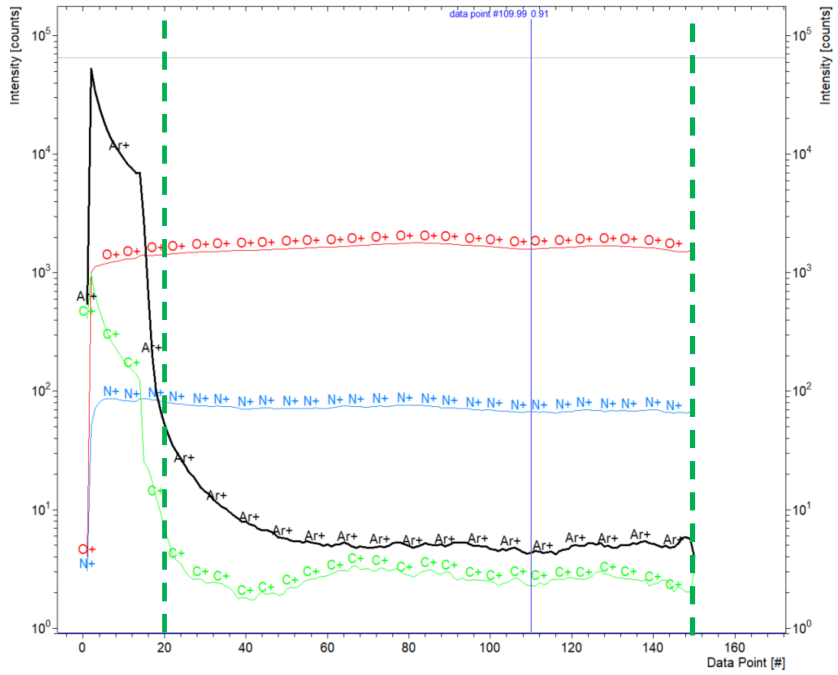

- **Oxygen** abundance ranking: **PB, PA, PC**
- **Argon** abundance ranking: **PA, PC, PB**
- **Nitrogen** abundance ranking: **PC, PB, PA**
- **Carbon** abundance ranking: **PA, PC, PB**

Fig 10. TOF-SIMS depth profile of O+, Ar+, N+, and C+ in sample PC-11, next to the abundance rating of all three samples.

The relatively small area tested during TOF-SIMS and measurement uncertainty of the chemical analysis using IGF make an unambiguous conclusion difficult. Oxygen distribution within the sample is also heavily influenced by the distribution of the oxide precipitate–forming elements like yttrium. For clarification, additional TEM of the initial powder particles should be performed to investigate the distribution of yttrium. STEM EDS maps were recorded for major and minor elements for sample PC-11 and are shown in two different magnifications in Fig. 11 and Fig 12. A cell structure along the print direction is visible with enrichments of nickel and aluminum and denuded iron. According to the phase diagram in Fig 1, a B2 NiAl phase can be assumed to have formed here with fast diffusion kinetics.

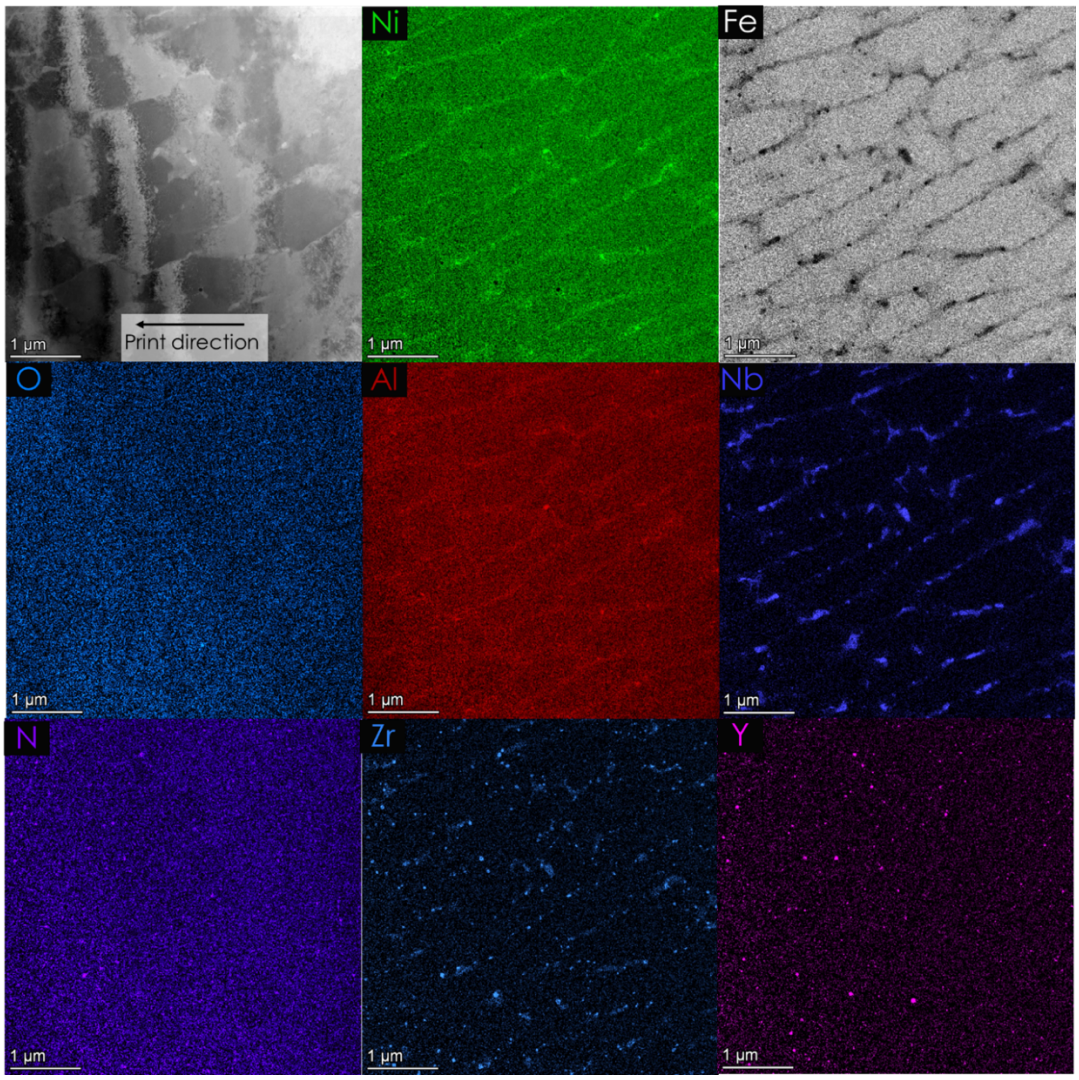

Fig. 11. STEM EDS maps of PC-11 at low magnification showing cell formation with nickel and aluminum enrichment. Spherical yttrium and zirconium precipitates are visible and not co-located.

Niobium is visible in similar areas, but instead of a continued enrichment along the formed cell structure, niobium-rich precipitates along the cell structure with sizes between 30 and 200 nm have formed. An increase in niobium from NAFA-1 to NAFA-2 was required to favorably increase the oxidation behavior but could result in intermetallic formation deteriorating the mechanical properties if not optimized in the future. Comparing the intended precipitate-forming elements zirconium and yttrium, it can be seen in Fig. 11 that zirconium is co-located along the cell structure, while yttrium seems to be homogeneously distributed throughout the material. As those precipitates are not co-located, an increase of sink strength due to a total increase in number densities of small precipitates is expected. In addition, a slight bimodal size distribution of precipitates could help with the creep properties of the material, as dislocations would require more energy to climb over increased precipitate sizes. This hypothesis needs to be proven in the future. However, the PC-11 sample clearly shows a route to successfully increasing the number density of precipitates during additive manufacturing of nano-precipitate steels.

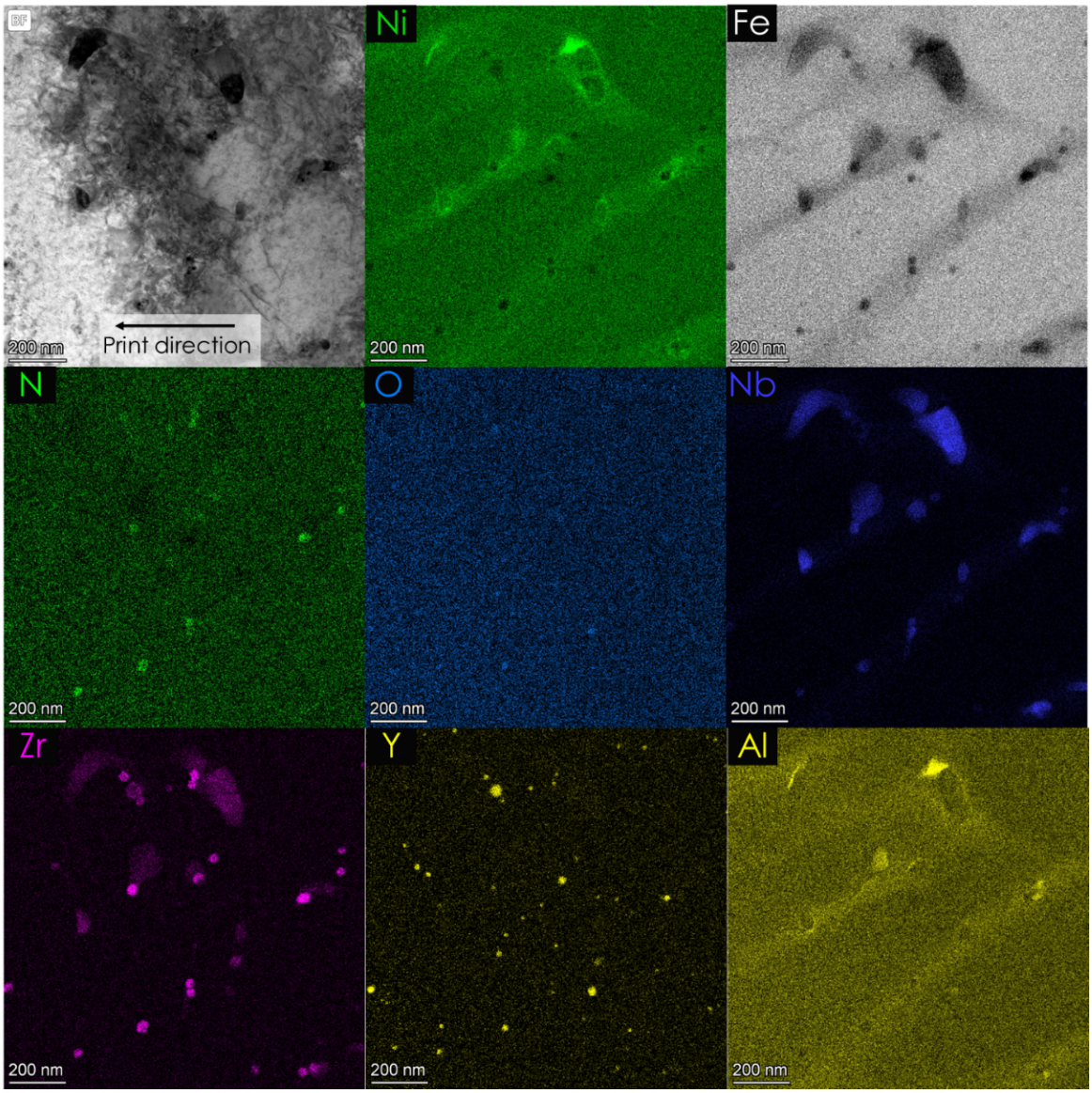

Fig 12. STEM EDS maps of PC-11 at higher magnification showing clearly the different locations of yttrium and zirconium precipitates.

4. POST-OXIDATION HIGH-TEMPERATURE PERFORMANCE

When these alloys are deployed in either fast-reactor or microreactor environments, it is important to validate that the compositions investigated can form a stable aluminum oxide surface layer to protect the material from potential fuel and/or coolant interactions. As such, initial scoping of these alloys has occurred following an annealing treatment for 1 h at 1000°C in air. Additional investigations in FY25 will include lower-length scale characterization to validate that the nanoscale features shown in this report are not significantly affected in reactor operating environments, but in this section, preliminary SEM microscopy and tensile results are highlighted.

Following heat treatment, a block of each sample (shown previously in Fig 6) was mounted and polished to a colloidal silica finish prior to secondary electron imaging. All samples had a highly adherent oxide layer measuring ~2 μm in thickness, as shown for sample PC-11 in Fig. 13 following the heat treatment. It is also important to note that this oxide layer remained intact regardless of the as-built surface roughness on the printed cubes, which was not polished or altered prior to the annealing treatment. As thick-walled tubes are eventually produced, and as the surface roughness is tuned to ensure that stress concentrators do not arise during subsequent pilgering steps, it is expected that the oxidation resistance will further improve.

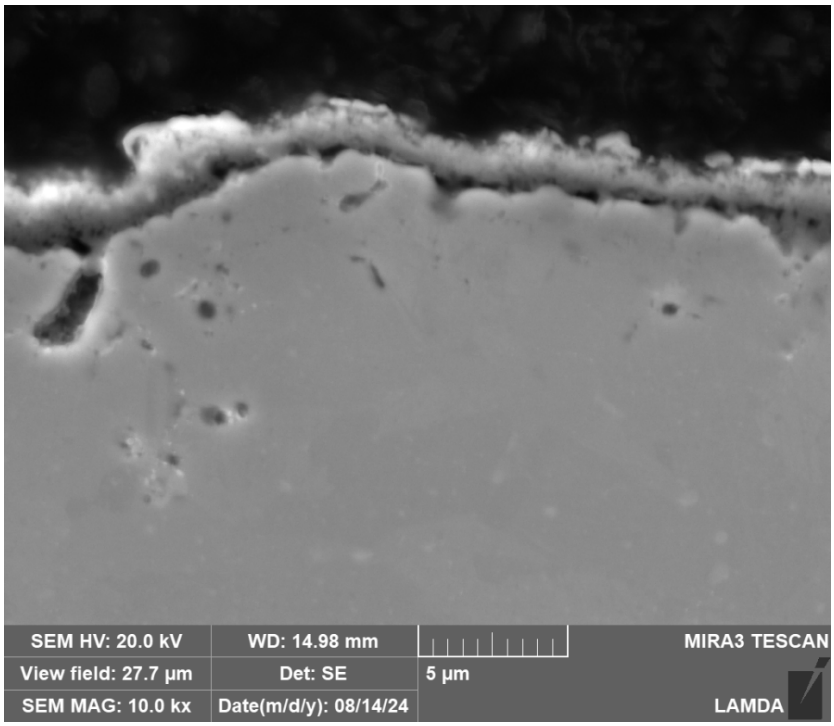

Fig. 13. SEM image of stable oxide layer formed on PC-11 following heat treatment at 1000°C for 1 h.

Tensile tests were also performed on PA, PB, and PC after heat treatment to investigate the impact of the dual precipitation mechanism in the material and the printing under nitrogen. SSJ3 tensile specimens were cut from the printed block with the stress axis parallel to the build direction. All three materials behave similarly at room temperature (RT) and the 600°C test condition, as shown in Fig. 14. It is readily apparent that these austenitic alloys have superior ductility in comparison with conventional ferritic alloys, while maintaining beneficial strength at higher operating temperatures. For example, a recently produced best practice heat of ODS alloy 14YWT for the Advanced Fuels Campaign (AFC) had a measured ultimate tensile strength of 425 MPa at 600°C, which is lower than that of PC-11 (617 MPa) measured in this work. Similarly, the LPBF NAFA alloy PC-11 has greater than 15% uniform elongation in comparison with less than 1% strain hardening capacity for the 14YWT alloy at the same test condition [14]. Thus, at elevated temperature operational conditions, these austenitic alloys have far superior mechanical strength (and prospective creep resistance) than their ferritic ODS counterparts.

However, there was not a significant difference in 0.2% yield strength (YS) or ultimate tensile strength (UTS) following annealing for the LPBF NAFA alloys regardless of printing atmosphere. It is clear from the prior EBSD results that these alloys have a similar large grain size, which is likely beneficial for creep resistance (minimal high-T grain boundary sliding), but this comes at a cost to lower-temperature Hall-Petch grain boundary strengthening. This potential explanation as to the similar mechanical performance is partially attributed to the similar grain size which, as shown in Fig 7, is very similar between all three materials. However, with differences in precipitation state, a larger variance in YS and UTS was expected between the inert (PA) and reactive environment (PB/PC) builds. Furthermore, the larger precipitates and cell structures could also have a large impact on the mechanical properties. We can assume that the precipitates did not pin the grain boundaries during printing, as they are not collocated, which indicates that the precipitates formed uniformly throughout the microstructure during rapid solidification, rather than being relegated to being co-located on high-angle grain boundaries. It is also unclear from these curves how significant thermally driven precipitate coarsening was in each printing condition, as well as if the high annealing temperature fully recovered the dislocation substructure that was shown to exist in the as-printed condition. These types of analyses will be performed in FY25 as we work to optimize the processing parameters of the NAFA tubes prior to working with partner institutions to produce tubes of the advanced austenitic alloys.

In addition to these high-T annealing treatments, a comparison between the materials regarding their irradiation behavior and thermal stability as well as creep properties would be relevant to show the difference between the materials. Additionally is it crucial to optimize the printing and minimize cracking during printing, as those could also lead to a statistically relevant error during the measurements.

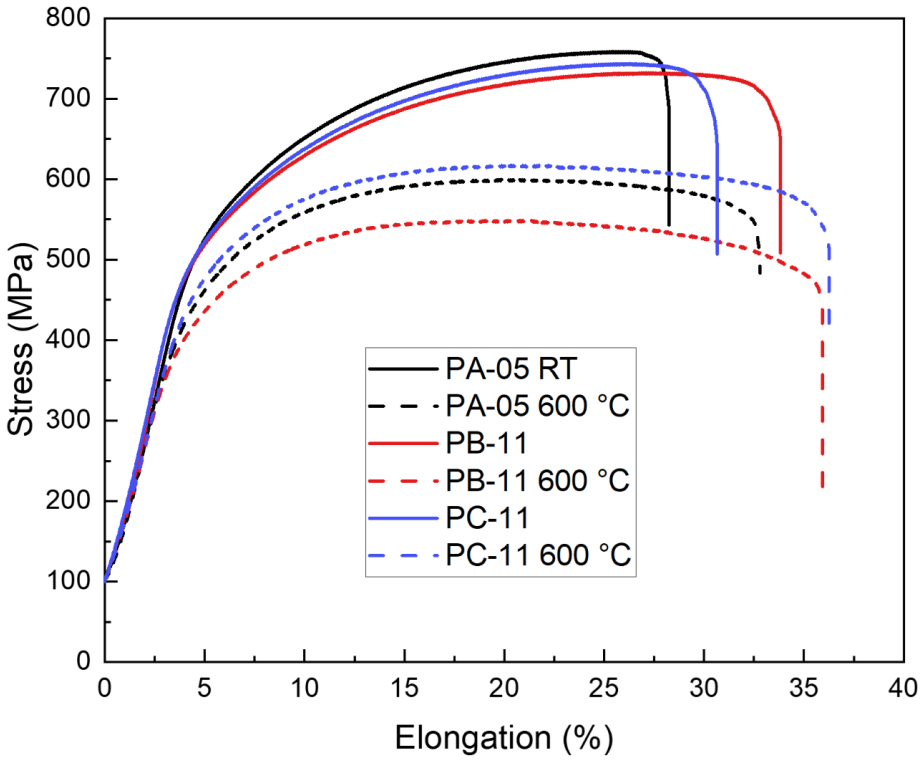

Fig. 14. Engineering stress vs elongation curves for PA-05, PB-11, and PC-11 tested at ambient temperature and 600°C.

5. CONCLUSIONS

The NAFA-2 microstructure was optimized to precipitate nitrogen-rich precipitates in addition to nano-sized oxide precipitates. Additive manufacturing under three different atmospheres with oxygen and nitrogen abundance has shown a successful formation of a dual precipitate–forming AFA material. Nitrides and oxides are not co-located and therefore increase the total number density of the precipitates, helping with irradiation resistance and embrittlement of the material. Even though the proof of concept was successful, more questions need to be answered to fully understand and optimize the complex microstructure toward application. Currently, the microstructure properties are dominated by the intermetallic phases formed during printing, as shown by the similar mechanical properties for all three tested materials. Long-term annealing of the material is needed to test the structural integrity during operation at elevated temperature. In addition, additive manufacturing of the material needs to be optimized further to reduce minor cracking within the printed blocks.

6. REFERENCES

[1] Y. Yamamoto, M.P. Brady, Z.P. Lu, P.J. Maziasz, C.T. Liu, B.A. Pint, K.L. More, H. Meyer, E.A. Payzant, "Creep-resistant, Al2O3-forming austenitic stainless steels," *Science* 316(5823), 433–436 (2007).

[2] B.A. Pint, Y.-F. Su, M.P. Brady, Y. Yamamoto, J. Jun, M.R. Ickes, "Compatibility of Alumina-Forming Austenitic Steels in Static and Flowing Pb," *JOM* 73(12), 4016–4022 (2021).

[3] A.G. Le Coq, D.A. Collins, N.G. Russell, R.H. Howard, H.C. Hyer, S.N. Dryepondt, C.C. Taylor, D.T. Hoelzer, C.P. Massey, *Status report on HFIR irradiation of optimized alumina forming alloys,* United States, 2024.

[4] Y. Yano, T. Uwaba, T. Tanno, T. Yoshitake, S. Ohtsuka, T. Kaito, "Tensile properties of modified 316 stainless steel (PNC316) after neutron irradiation over 100 dpa," *Journal of Nuclear Science and Technology* 61(4), 521–529 (2023).

[5] C. Massey, D.T. Hoelzer, Y. Yamamoto, T.G. Seibert, S. Dryepondt, H. Hyer, J. Kendall, M. Zach, *Progress on Design and Production of Oxide Dispersion–Strengthened Alumina-Forming Austenitic Alloys for Nuclear Applications*, Oak Ridge National Laboratory (ORNL), Oak Ridge, TN (United States), 2023.

[6] T. Seibert, S. Dryepondt, H. Hyer, C. Massey, J. Kendall, D. Hoelzer, Y. Yamamoto, S. Nayir, *Nanostructured Alumina Forming Austenitic Alloy (NAFA) production using mechanical alloying and high-temperature consolidation* (2024).

[7] T. Horn, C. Rock, D. Kaoumi, I. Anderson, E. White, T. Prost, J. Rieken, S. Saptarshi, R. Schoell, M. DeJong, "Laser powder bed fusion additive manufacturing of oxide dispersion strengthened steel using gas atomized reaction synthesis powder," *Materials & Design* 216, 110574 (2022).

[8] L. Autones, P. Aubry, J. Ribis, H. Leguy, A. Legris, Y. de Carlan, "Assessment of Ferritic ODS Steels Obtained by Laser Additive Manufacturing," *Materials* 16(6), 2397 (2023).

[9] S. Saptarshi, M. DeJong, C. Rock, I. Anderson, R. Napolitano, J. Forrester, S. Lapidus, D. Kaoumi, T. Horn, "Laser Powder Bed Fusion of ODS 14YWT from Gas Atomization Reaction Synthesis Precursor Powders," *JOM* 74(9), 3303–3315 (2022).

[10] H. Jia, Z. Zhou, S. Li, "A new strategy for additive manufacturing ODS steel using Y-containing gas atomized powder," *Materials Characterization* 187, 111876 (2022).

[11] T. Gräning, M. Rieth, J. Hoffmann, A. Möslang, "Production, microstructure and mechanical properties of two different austenitic ODS steels," Journal of Nuclear Materials 487, 348–361 (2017).

[12] J. Chen, P. Jung, T. Rebac, F. Duval, T. Sauvage, Y. De Carlan, M. Barthe, "Helium effects on creep properties of Fe–14CrWTi ODS steel at 650°C," *Journal of Nuclear Materials* 453(1–3), 253–258 (2014).

[13] P. Edmondson, C. Parish, Q. Li, M. Miller, "Thermal stability of nanoscale helium bubbles in a 14YWT nanostructured ferritic alloy," Journal of Nuclear Materials 445(1–3), 84–90 (2014).

[14] C. Massey, D.T. Hoelzer, *Characterization of Large Batch 14YWT Heat (NFA-2) for JOYO Irradiations*, United States, 2024.